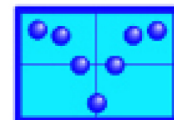
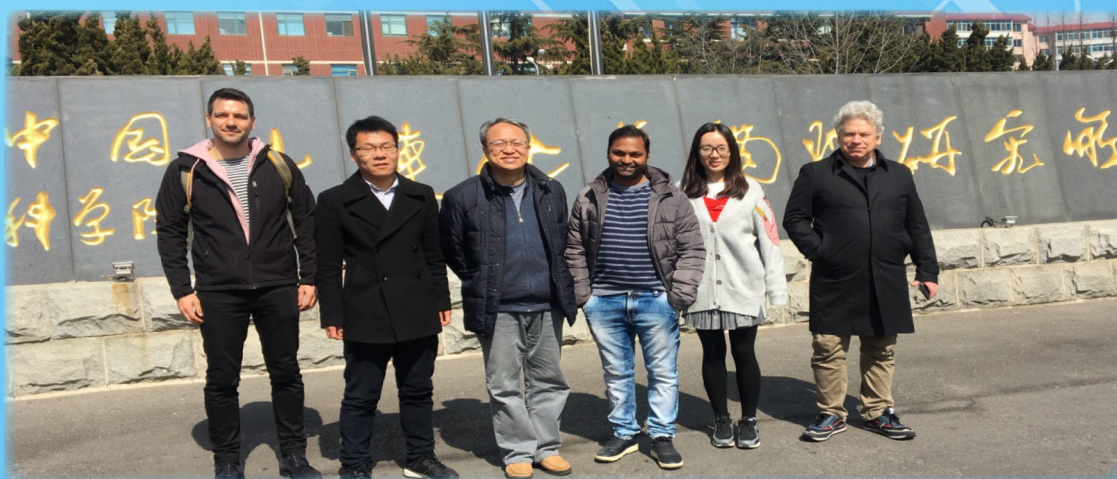
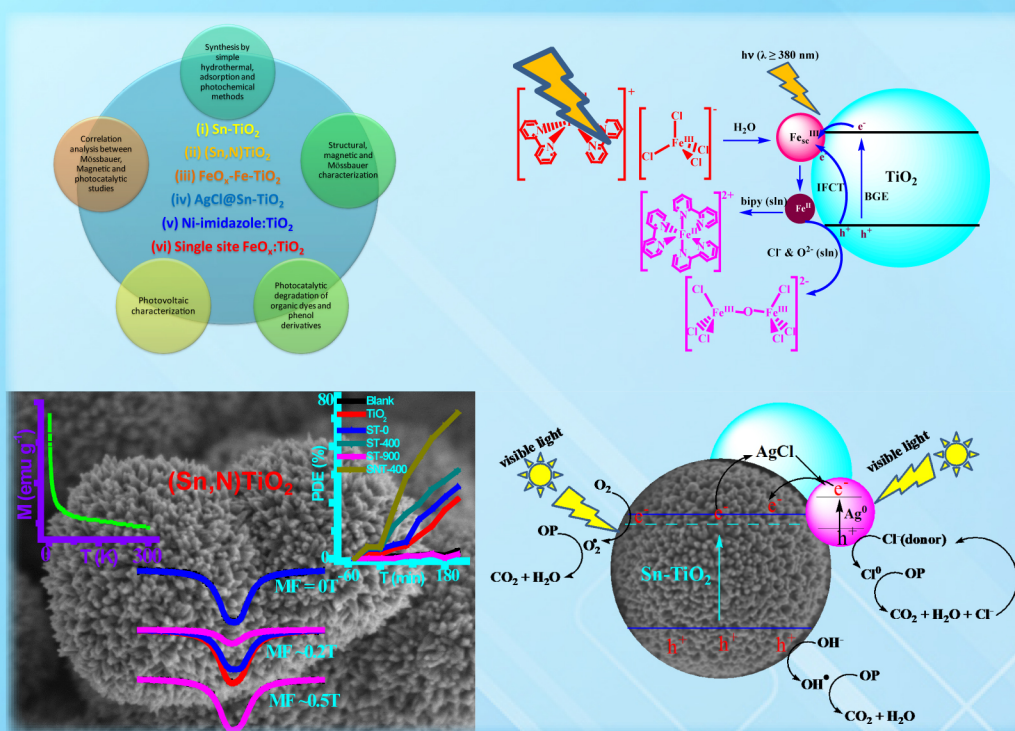


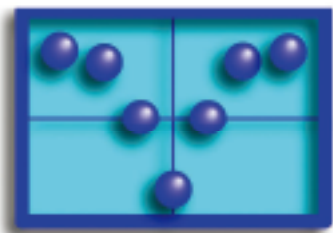
Mössbauer Effect Reference and Data Journal



March 2018 • Volume 41 • Number 1

Mössbauer spectroscopic, magnetic and photocatalytic investigations of tin or iron-based titania nanocomposites





MÖSSBAUER SPECTROSCOPY NEWSLETTER

March 2018

Mössbauer spectroscopic, magnetic and photocatalytic investigations of tin or iron-based titania nanocomposites

Ayyakannu Sundaram Ganeshraja^(✉), Junhu Wang^(✉)

Mössbauer Effect Data Center, Dalian Institute of Chemical Physics, Chinese Academy of Sciences, Dalian 116023, China.

Email: asgchem84@gmail.com, wangjh@dicp.ac.cn

Abstract

Mössbauer spectroscopic, magnetic and photocatalytic investigations on bulk and supported tin or iron-based titania nanocomposites were reviewed. Following two efficient methods are used for preparing highly efficient tin or iron-based titania photocatalysts: (i) (M, Sn)TiO₂ (where M = N and AgCl) nanocrystals were designed and produced by simple hydrothermal method, and (ii) FeO_x-TiO₂ nanocrystals were prepared by novel photochemical method, in which visible light are mediated reduction of surface bound ionic type iron(III)-bipyridyl complex on TiO₂ surface. The chemico-physical properties were characterized by various conventional techniques, the structure-activity relationships, magnetic and photocatalytic mechanism of nanocrystals was mainly explored by Mössbauer spectroscopic technique under various simulated working conditions. However, the magnetic property depends critically on oxygen vacancy, structural defects, chemical states of Fe or Sn and content. In this review, we present the state-of-the-art development of fabrication strategies, Mössbauer spectroscopic and magnetic investigations of Sn or Fe-based titania nanocomposites and their corresponding photocatalyst application.

Biography

Dr. A. S. Ganeshraja, Postdoctoral



Researcher in Mössbauer Effect Data Center, Dalian Institute of Chemical Physics, Chinese Academy of Sciences from August, 2014 to still. He was born in 1984. He received Ph.D degree in chemistry from the Pondicherry University, India in 2014. He has published several research papers (32 no. current status) in refereed international journals and awarded the CAS President's International Fellowship Initiative program in year 2016. He has granted NSFC research fund for International Young Scientists funded by National Natural Science Foundation of China. He has recently published number of research papers on the development of ferromagnetic metal oxide coupled photocatalysts. Currently, he is working on "Mössbauer active ferromagnetic single site metal oxide coupled photocatalysts".



Junhu Wang is a Professor of Chemistry, main research fields are Mössbauer spectroscopic applications and nanometer catalytic materials. He was graduated from

Radiochemistry Major, Lanzhou University in 1991. He was awarded the master's and doctor's degrees (jointly trained with Japan Atomic Energy Research Institute) of Toho University (Japan) in 1998 and 2002, respectively. He holds many titles and awards, such as full professor & group leader of Dalian Institute of Chemical Physics (DICP), Chinese Academy of Sciences (CAS), winner of "Hundred Talents Program" honor of introducing outstanding talents from abroad and the financial incentives, Secretary-general of Mössbauer Effect Data Center (MEDC), Executive Editor of Mössbauer Effect Reference and Data Journal (MERDJ), Executive Chairman of 8th International Symposium on the Industrial Applications of the Mössbauer Effect, Member of Councils of China Nuclear Physics Society (CNPS) and Chinese Mössbauer Community. Advisor Member of International Board on the Applications of the Mössbauer Effect (IBAME), Members of American Chemical Society (ACS) and Chinese Chemical Society (CCS). Over the years, he served at Tokyo National University of Fine Arts and Music (Japan), National Institute for Materials Science (NIMS), National Institute of Advanced Industrial Science and Technology (AIST), and Chukyo University for scientific research and teaching. Current Research Interests: 1) Novel and highly efficient environmental & energy catalytic materials; 2) Novel and highly efficient reactive adsorption materials; and 3) The development and applications of in-situ advanced spectroscopic techniques.

1. Introduction

Metal oxide semiconductor (MOS) has been fervently researched over the past few decades due to its potential applications across many different areas. In particularly titania based semiconductor has seen considerable use as a white pigment in paint, food coloring, and personal care products and as a UV absorber in sunscreens [1]. While, TiO_2 including some other MOS such as SnO_2 , and ZnO have been commonly regarded as benchmark photocatalysts and their role in this area has been substantially studied for several decades. They show special properties such as enhanced photoluminescence, chemical and photochemical reactivities [2]. However, pristine TiO_2 alone have an inherent and significant drawback: the photogenerated charge carriers (electron-hole pairs) could

recombine rapidly [3]. Therefore, to increase the photocatalytic activity of TiO_2 , it is important to suppress the recombination of photogenerated charge carriers. A variety of approaches have been applied to improve the photocatalytic activity of TiO_2 . One interesting approach is to couple the TiO_2 with other semiconductor material with different energy levels, which suppresses the recombination of photogenerated charge carriers in a semiconductor system and thus improving the efficiency of net charge transfer at the semiconductor/electrolyte interfaces [4]. Many other approaches are used to improve the photocatalytic property of titania such as doping, codoping, grafting, grafting/doping methods. Based on literature studies tin containing titania nanocomposite materials could alter the photocatalytic as well as magnetic behaviors which was investigated by Mössbauer technique. Mössbauer spectroscopy, a powerful technique that is able to give account of structural features for all iron or tin species taking part in the catalysis process, is considered to be a crucial technique for determining catalyst phase, identifying active site, and investigating correlations between catalytic behavior and the coordination structure of catalysts, which are highly desirable for clarifying the catalytic mechanisms [5]. This technique also tool to investigate the magnetic behavior and defect structure of iron or tin containing MOS.

In our previous research related to the magnetic and photocatalytic activity, and Mössbauer spectroscopic analysis of tin or iron-based titania photocatalysts such as metal oxide coupled TiO_2 [6], Sn-TiO_2 nanocrystals [7], iron oxide coupled and doped TiO_2 [8], nickel-imidazole// TiO_2 [9], hierarchical $(\text{Sn}, \text{N})\text{TiO}_2$ [10] and $\text{AgCl}@(\text{Sn}, \text{N})\text{TiO}_2$ [11] microspheres. Moreover, we recently reported [12], the near-UV and visible light induced interfacial electron transfer (IFET) process between aqueous solution of $[\text{Fe}(\text{bipy})_2\text{Cl}_2][\text{FeCl}_4]$ complex and TiO_2 NPs has been proved by ^{57}Fe Mössbauer spectroscopic method. Based on our previous reports, herein we write short review about Mössbauer, magnetic and photocatalytic investigations of Sn or Fe-based titania nanocomposites. The latest synthesis methods and recent progress in the photocatalytic applications of Sn or Fe-based titania nanocomposite materials are reviewed.

2. Sn-TiO₂ Nanocrystals

2.1 Preparation of Sn-TiO₂ Nanocrystals

Firstly, 5 mol precipitates of titanium(IV) hydroxide prepared by 5 mL titanium isopropoxide and concentrated ammonium hydroxide (30%, 50 mL) in water were dissolved into nitric acid (6 M, 50 mL) and hydrogen peroxide (30%, 5 mL) to produce a reddish brown titanium(IV) nitrate solution. Then 0.05, 1.5, 2.0, 3.0 and 4.0 mL SnCl₄ (1 M in methylene chloride) solutions were separately added into the titanium nitrate solutions under magnetic stirring for the preparation of various Sn loaded TiO₂. Then 100 mL oxalic acid solutions (0.6 M) were separately introduced drop wise within 2 h under magnetic stirring to ensure complete precipitation. The resultant mixtures were transferred into Teflon lined stainless steel autoclave, sealed and heated at 110 °C for 4 h with the pressure maintained at 18 psi. Finally, the precipitates were filtered, washed with distilled water and ethanol, and dried in air at 90 °C for 12 h. The dried precipitates were calcined at 400 °C for 4 h in a muffle furnace to get Sn-TiO₂ photocatalysts. The undoped anatase TiO₂ sample was synthesized by the same process except without addition of SnCl₄ precursor. Hereafter, the Sn doped TiO₂ samples were denoted as Sn-Ti-x (x represents the atom ratio % of Sn/Ti, x = 0 - 1.37). The complete experimental details already reported in our previous paper [7].

2.2. ¹¹⁹Sn Mössbauer spectroscopic investigation of Sn-TiO₂ nanocrystals

The Sn-Ti-x samples were prepared by simple hydrothermal and calcinations processes in line with our recent article which also outlined the structural, morphology, physicochemical and photocatalytic properties of Sn-Ti-x samples [7]. The catalytic properties studied include (i) the formation of anatase, mixed anatase-rutile, and rutile phases with increasing Sn level in Sn-doped TiO₂, (ii) the enhanced light absorption property in the visible region, (iii) Sn content in TiO₂ assisted magnetic characters and (iv) photocatalytic activities showing structural, luminescent and ferromagnetic dependences [7]. Figure 1 presents the ¹¹⁹Sn Mössbauer spectra of the Sn-Ti-x samples at room temperature. Mössbauer spectra of low level Sn doped TiO₂ samples were decomposed into a doublet and a sextet and Mössbauer spectra of high level doped samples into one more sextet magnetic

component because almost all samples showed the weak ferromagnetism. We obtained interesting inner magnetic fields of around 3T from ¹¹⁹Sn Mössbauer spectra of low Sn doped TiO₂. The doublet and magnetic sextet are considered due to paramagnetic Sn doped TiO₂ and defect induced magnetism, respectively. It is reasonable that all isomer shift values near the 0.0 mm/s show the valence states of Sn⁴⁺ because Ti has also valence state of 4+. The ionic radius of Sn⁴⁺ (69 pm) is larger than that of Ti⁴⁺ (53 pm). The high Sn doped samples showed the more broadened Mössbauer spectra. We decomposed them by adding one more magnetic sextet component. The XRD and transmission electron microscope data of the highly Sn doped TiO₂ samples showed the rutile structure of TiO₂ and the trace level of rutile SnO₂ [7]. More complex structure of the powder grains was observed, which may be due to different configurations of Sn(Ti)O₂ with structural defect sites or with 2Ti atoms substituted at 2Sn atom sites. More precisely, isomer shift (IS) are found to be positive values, which are consistent with the values reported for the Sn⁴⁺ dopant in transition metal oxides [13, 14]. This fact thus suggests the occurrence of Ti-O-Sn-O-Ti chain fragments in the lattice and, consequently, insertion of dopants into the matrix [14]. The doublet having large IS and quadrupole splitting (QS) is associated with defects and vacancies that are stabilized by doping of Sn⁴⁺ in TiO₂ lattice. However, the IS value of the sample with x = 1.37 is rather small, which may show the partial product of precipitated nanosized SnO₂.

2.3. Magnetic investigation of Sn-TiO₂ nanocrystals

The field dependence of magnetizations for Sn-Ti-x samples was measured at room temperature are shown in Figure 2. Significant hysteresis loops in the M-H curves indicated the weak room temperature ferromagnetic (RTFM) behavior observed (Figure 2a) for anatase Sn-Ti-x (x = 0, 0.05 and 0.12) and ferromagnetism (FM) with diamagnetic (DM) behaviors observed for remaining samples (Figure 2b). The M_s values were increased from 10.3 to 129.6 memu for increasing x from 0 to 0.12, it could be due to spin reorientation arising from spin-spin interaction between Sn-O and Ti-O dipoles [15]. This implies that the interface has an additional effect on magnetism. There can be a large amount of lattice mismatch at the interface in Sn-Ti-x

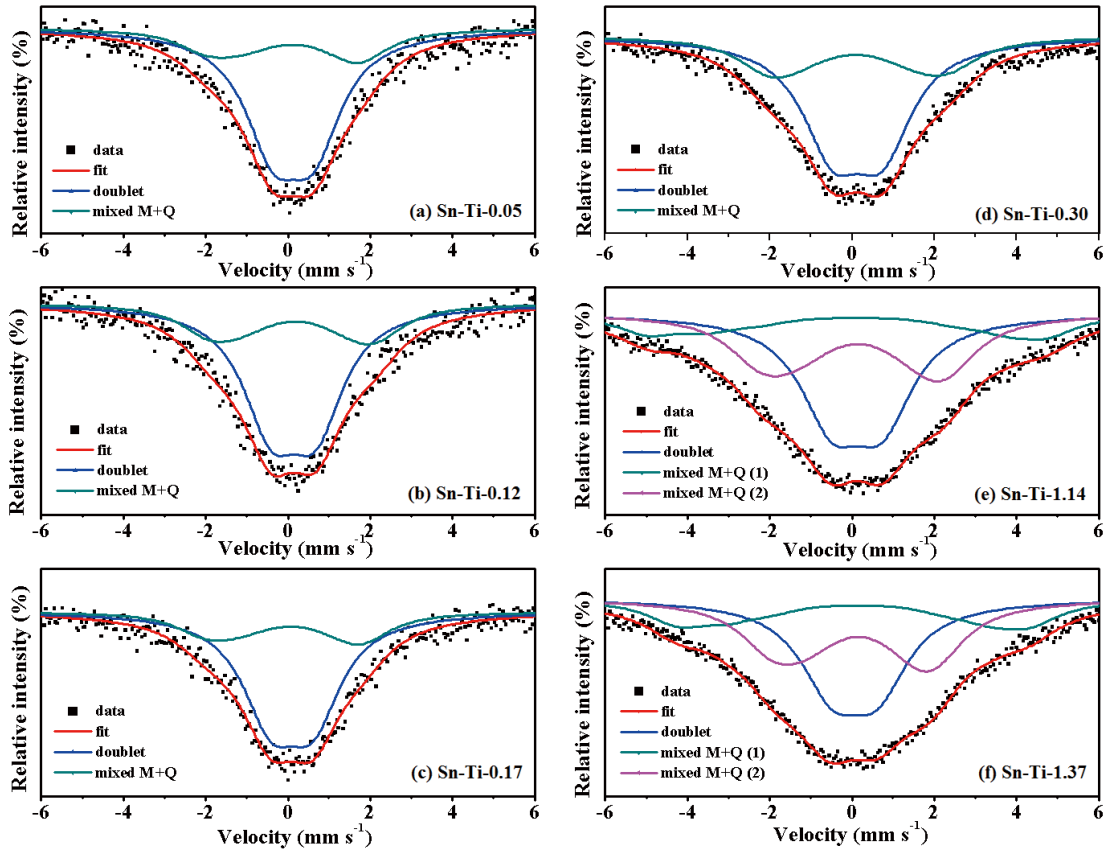


Figure 1. Room temperature ^{119}Sn Mössbauer spectra of Sn/Ti-x(%) samples.

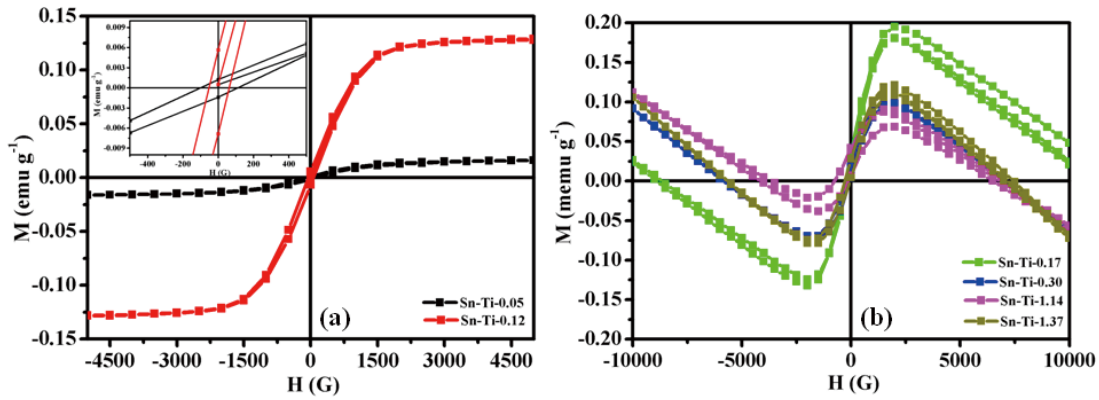


Figure 2. Magnetic hysteresis loops of Sn-Ti-x (a) $x = 0.05$ and 0.12 and (b) $x = 0.17, 0.30, 1.14$ and 1.37 samples at room temperature, the inset gives the enlarged M-H curves between 500 and $+500$ G.

samples with a high possibility of presence of uncompensated bonds of Sn, Ti and O. The FM interaction in TiO_2 is weaker than SnO_2 ; hence the spins at the interface layer come across two different kind of interaction. FM interaction of SnO_2 might extend the interaction in TiO_2 via Ti vacancies and hence increase M_r . This extension of FM interaction should also be the reason of enhanced M_s in Sn-Ti-x samples. The pristine SnO_2 sample reported the DM behavior [16, 17] with the

very weak FM signal resulting possibly from native defects [18, 19], while the Sn-Ti-x ($x = 0.17, 0.30, 1.14$ and 1.37) displays the mixture of DM and FM behaviors as shown in Figure 2b. It can be concluded that the observed magnetic properties are nature and the FM and DM signals are due to the incorporation of Sn^{4+} ions in TiO_2 host matrix. Therefore, when the magnetic moments are very weak for Sn-Ti-x samples, the intrinsic DM back ground of SnO_2 takes dominant status again.

2.4. Correlation of magnetic vs photocatalytic behavior of Sn-TiO₂ nanocrystals

In Figure 3, the relative area intensity of paramagnetic Sn doped TiO₂ (doublet) sites, magnetic components (sextet 1 and sextet 2), the saturation magnetization (M_s) and coercive field (H_c) values of bulk magnetism, and the photocatalytic activity PDE were plotted for various x (Sn/Ti (%)). The M_s and H_c values published in our previous paper [7] are used herein. The intensity of paramagnetic doublet of Sn⁴⁺ was found to decrease with increasing x ; however, opposite behavior was observed for magnetic components. Moreover, the PDE were compared with the intensity of the paramagnetic doublet. It is likely that paramagnetic Sn species influenced the photocatalytic activity due to the stabilization of the electronic excitation energy level. The higher amounts of structural defects are likely related to the induced magnetism rather than photocatalytic activity. Irregular behavior was

observed for Sn-Ti-0.30 sample, which may decrease its photocatalytic activity due to the inhibition of the carrier transformer between rutile and anatase phases. Furthermore, the very low level Sn doped samples (Sn-Ti-0.05 and Sn-Ti-0.12) showed high magnetism, which might be due to the deformed anatase structure, whereas the high photocatalytic activity was kept because the diluted Sn doping did not affect the anatase phase transformation. The H_c increased with the increase of doped Sn concentration, which shows that the H_c may be strongly correlated with the mixed phases and structural defects. It was concluded that the low level Sn doping into anatase TiO₂ stabilizes the electronic excitation energy level and the electron transfer under irradiation, whereas the high level Sn doping induced the mixed phases and magnetic defects at the interfaces states. Hence the RTFM should be extended to various potential applications, such as spintronics, photodegradation, catalysis, separation, and purification processes.

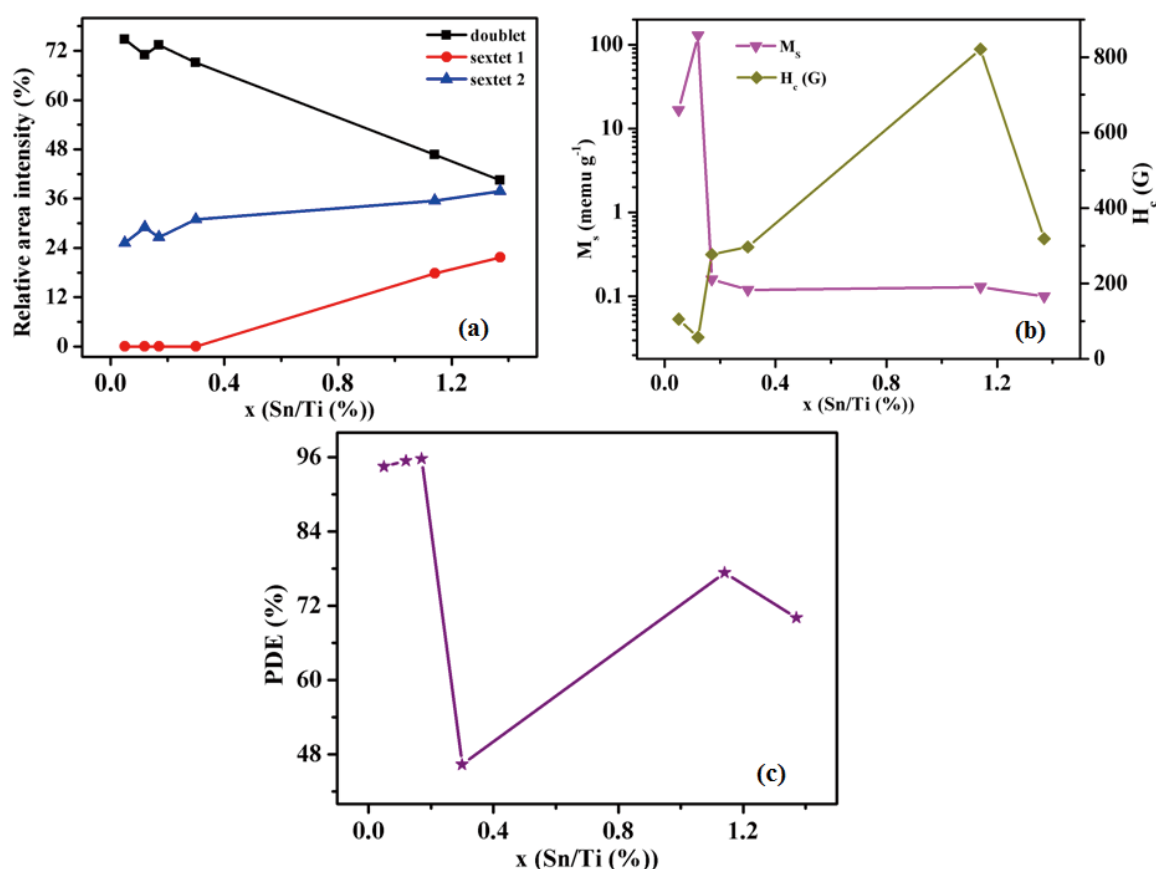


Figure 3. Variation of relative area intensity of doublet, sextets 1 and 2 obtained from ¹¹⁹Sn Mössbauer measurements (a), saturation magnetization (M_s) and coercivity (H_c) obtained from room temperature vibrating sample magnetometer (VSM) (b) and PDE values (at 120 min) (c) with various atomic ratios (x = Sn/Ti (%)) of Sn-Ti- x samples.

3. Hierarchical (Sn,N)TiO₂ microspheres

3.1. Preparation of Sn and N codoped TiO₂ microspheres

The Sn-TiO₂ samples were prepared and denoted as ST-x (x represents the various calcinations temperature at 400 and 900 °C, x = 0 is non-annealed sample) in our previous paper [7, 10]. The resulting ST-0 sample was placed in a quartz boat. This boat was then placed in a quartz tube with airtight, stainless steel end-caps that have welded valves and connections to input and output gas lines. The quartz tube was then placed in a tube furnace, and the appropriate connections to the gas sources were made. An argon gas flow through the tube was used for 15 min to expel the air remaining in the tube before establishing the flow of ammonia gas through the tube. The sample was then heated in the tube to 400 °C at 4 °C/min speed, respectively. After 4 h calcination, the furnace power was turned off and the product was cooled to room temperature in 4 h under an ammonia gas flow. Before the quartz tube was taken out of the tube furnace, an argon gas flow through the tube was used

to expel the ammonia gas remaining in the tube. The Sn and N codoped TiO₂ sample was denoted as SNT-400.

3.2. Magnetic property of Sn-TiO₂ and (Sn, N)TiO₂ microsphere

In our previous paper [10], hierarchical tin-doped titania (ST) and tin- and nitrogen codoped titania (SNT) microspheres were prepared and characterized by a hydrothermal method and nitriding treatment, in particular, SNT-enhanced visible light photocatalytic activity for the degradation of rhodamine B in aqueous solution and room-temperature ferromagnetism (RTFM). However, the magnetic response was measured as a function of magnetic field strength (M–H) at 300 and 2 K. Figure 4a, b shows the hysteresis loops of pristine TiO₂, ST-x and SNT-400 samples. It indicates that all samples have weak ferromagnetic nature at room and low temperatures. Among all samples ST-0 showed high magnetic response at room temperature; it may be due to generation of amorphous nature, oxygen vacancies and structural defects

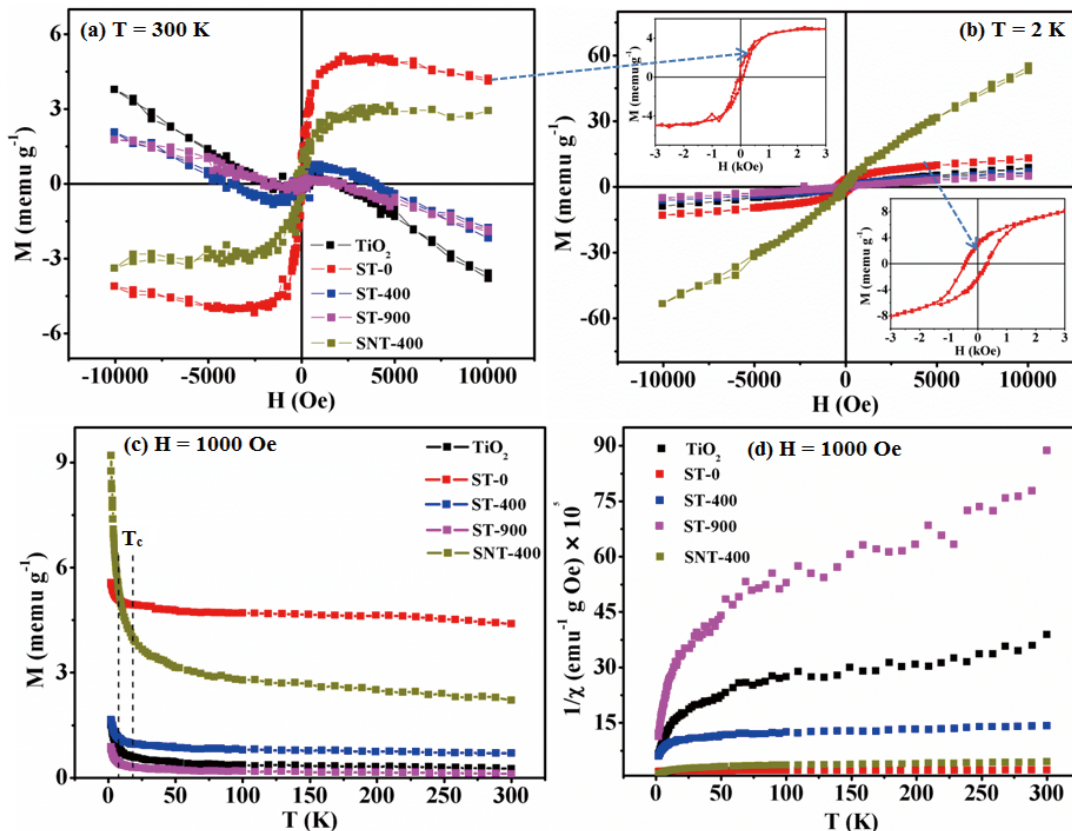


Figure 4. Magnetization curve of pristine TiO₂, ST-x and SNT-400 samples at 300 K (a) and 2 K (b) and visible hysteresis loop of ST-0 at 300 and 2 K (insert figures), temperature dependence of magnetization plots measured temperature range from 2 to 300 K (c) (where the critical phase transition temperature (T_c)), and variation in inverse magnetization with temperature (d).

induced magnetism. We observed weak and hard FM hysteresis loops for ST-0 sample at room (300 K) and low (2 K) temperatures (Figure 4b insert), respectively. To further explore the magnetic behavior of the ST-x and SNT-400 samples, the temperature dependence of the magnetization (M-T) for ST-x and SNT-400 samples was measured as shown in the Figure 4(c, d). This indicates that these samples have a temperature dependent magnetic property. Previous reports have attributed to the RTFM in Sn-doped TiO_2 [7] and N-doped TiO_2 due to V_o (defects) induced magnetism [21]. Similar property was observed in our present samples and V_o or structural defects play a dominant role in increased magnetic behavior of ST-x and SNT-400 microspheres. The SNT-400 samples showed strong ferromagnetic/superparamagnetic character at room and low temperatures.

3.3. ^{119}Sn Mössbauer spectroscopic investigation of Sn- TiO_2 and (S, N) TiO_2 microspheres

^{119}Sn Mössbauer spectroscopy is important tool to understand the microstructures and magnetic behaviors of Sn based catalysts. Figure 5 present the interesting results on the ^{119}Sn Mössbauer spectra of all as-prepared samples in absence of magnetic field (MF) as well as in presence of weak (~ 0.20 T) and strong external MF (~ 0.50 T). ^{119}Sn Mössbauer spectra of all samples decomposed into a doublet and a sextet in presence of weak

MF, while the doublet has more predominant component than sextet. Even we can identify single doublet in absence of MF. However, Mössbauer spectra were significantly broaden under the external field, and identified as a magnetic sextet in presence of strong external MF. It indicates that the Sn sites have behavior of the magnetic relaxation/splitting in presence of external MF. It is reasonable that all isomer shift values near the 0.0 mm s^{-1} show the valence states of Sn^{4+} because Ti has also valence state of $4+$. Hence, Sn^{4+} ions easily substituted into Ti^{4+} lattice in bulk TiO_2 . Our previous paper reported that the doublet and magnetic sextet of various Sn content in TiO_2 nanocrystals were considered as two Sn sites as Sn^{4+} doped into bulk and defect induced magnetism of TiO_2 , respectively [21]. In this work, ^{119}Sn Mössbauer analysis of hierarchical ST and SNT microspheres at different calcinations, the ^{119}Sn Mössbauer spectra of all samples showed a sextet with considerable relative intensity (4.6 - 14.8 %) in presence of weak external MF. However, the paramagnetic species shows doublet with IS values from 0.11 to 0.16 mm s^{-1} , which corresponds to paramagnetic Sn^{4+} substituted into Ti^{4+} sites, while large IS values are associated with defects and vacancies that are stabilized by doping of Sn^{4+} in TiO_2 lattice [22]. The sextet magnetic component was clearly observed in the presence of strong MF. Here we observed almost all same IS, although different QS values in absence and presence of strong MF. The large QS values for non-magnetic

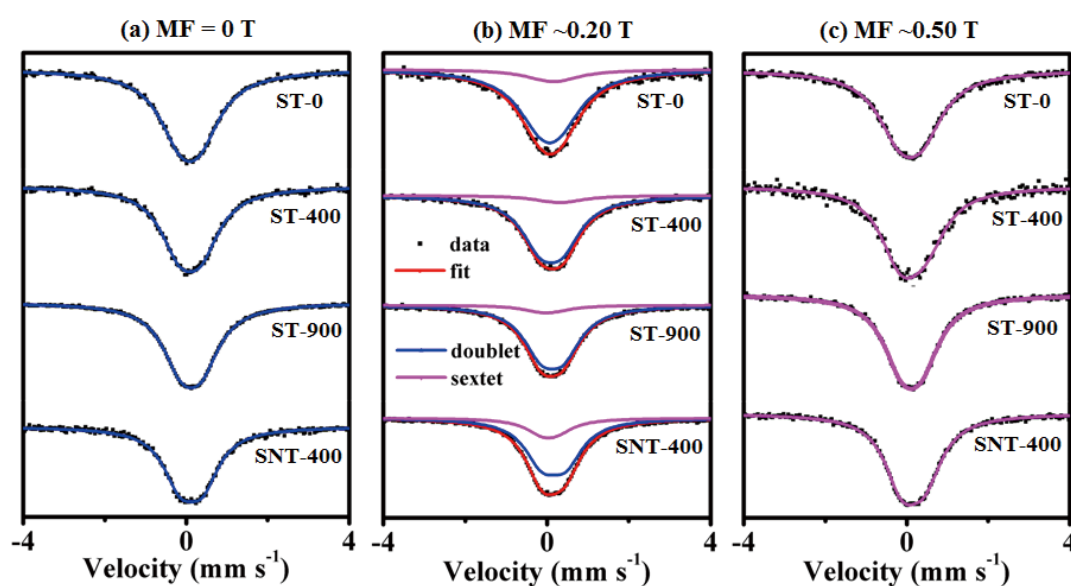


Figure 5. Room temperature ^{119}Sn Mössbauer spectra of ST-x and SNT-400 samples in absence (a) and presence of weak (b) and strong (c) external magnetic fields.

component explore the defects sites presented in all as prepared samples. The defect sites are origin for observed ferromagnetic character in MOS. Thus it is considered that the double exchange interaction result in the ferromagnetic behavior. Hence, nearby Ti and Sn atoms share a V_o , which concludes that V_o play an important role in the ferromagnetic property, enhancing the magnetic moments and favoring the ferromagnetic coupling between Ti and Sn atoms. Hence, the sextet may come from the magnetic relaxation of spin-lattice interaction [21]. It is considered that since the SNT-400 samples had large amount of sextet component (14.8 %) among all other as-prepared samples, it showed good magnetic and photocatalytic behaviors [10].

4. Hierarchical AgCl@Sn-TiO₂ microsphere

4.1. Preparation of hierarchical AgCl@Sn-TiO₂ microsphere

The AgCl@Sn-TiO₂ microspheres were obtained by single step process. This preparation process was slightly modified from our previous reports [6, 7]. Initially, 5 mol reddish brown titanium nitrate solutions were prepared [6] and then 0.50 mL SnCl₄ (1 M in methylene chloride) followed by 0.01, 0.05, 0.10 or 0.50 M AgNO₃ (50 mL) solutions were added into the titanium nitrate solutions under magnetic stirring. Then 100 mL oxalic acid solutions (0.6 M) was introduced drop wise within 4 h under magnetic stirring and the resulting solution was kept in dark place at room temperature for 48 hours. The resultant mixtures were transferred into 500 mL reagent bottle, sealed and heated at 121 °C for 3 h with the pressure maintained at 15 psi. Finally, the precipitates were filtered, washed with distilled water and ethanol, and dried in air at 90 °C for 12 h. The dried precipitates were calcined at two different temperatures such as 400 and 900 °C for 4 h in a muffle furnace to get AST microsphere. Hereafter, the AgCl@Sn-TiO₂ with different AgCl content level and samples post-annealed at various temperatures were denoted as AST-x-y (where “x” represents various concentrations such as 0.01, 0.05, 0.10 or 0.50 M of AgNO₃ solution used in preparation method and “y” represents the various calcination temperatures such as 400 and 900 °C, y = 0 is non-annealed sample).

4.2. Photocatalytic performance

Figure 6a shows the evolution of the

absorption of RhB with light irradiation time on the AST-0.50-400 microspheres. It can be seen that RhB was degraded efficiently by the AST microsphere (10 mg of catalyst used in 80 mL RhB aqueous solution) under visible light ($\lambda \geq 420$ nm), and after 90 min of irradiation time, almost all RhB has been decomposed. Prior to irradiation, the RhB solution over the catalyst was kept in the dark for 30 min to obtain the equilibrium adsorption state. In the dark, no reaction occurred in any system, and the adsorption amount was negligibly small (Figure 6b). As the irradiation time increases, the decomposition of RhB progresses steadily, and decomposition over the AST-0.50-400 catalyst is completed in 90 min of visible-light irradiation. Supposed that the photodecomposition of much diluted aqueous solution of RhB has a pseudofirst-order reaction mechanism, the rate constant of the RhB decomposition over AST-0.50-400 is estimated to be about 0.041 min⁻¹, faster than that over P25 (ca. 0.009 min⁻¹), AgCl (ca. 0.006 min⁻¹) and Ag/AgCl (ca. 0.008 min⁻¹), further we could compare with our previous reported photocatalysts of Sn-TiO₂ and (Sn, N)TiO₂ (ST-0 (ca. 0.002 min⁻¹), ST-400 (0.004 min⁻¹), ST-900 (0.001 min⁻¹) and SNT-400 (0.007 min⁻¹) microspheres. However, AST-0.50-400 sample has excellent photocatalytic performance than any as-prepared samples (Figure 6b). These experimental results clearly demonstrate that the synthesized hierarchical AST microspheres could serve as a type of photocatalyst for the efficient degradation of dye pollutants.

To fully understand the photocatalytic property of the AST microspheres, the possible mechanism of photocatalytic degradation of organic pollutant on the hybrid was proposed in Figure 7. Electron-hole pairs are generated by the band gap excitation of Sn-TiO₂ [7]. Excited electron flow through conduction band of Sn-TiO₂ to AgCl to form Ag⁰ [23, 24]. For the AST samples, Sn-TiO₂, having a smaller band energy gap than that of AgCl [25, 26], can absorb more visible light ($\lambda \geq 420$ nm), which generates more electrons to improve the photoreduction reaction. The detailed photocatalyst reaction mechanism was reported in our paper [11].

4.3. ¹¹⁹Sn Mössbauer and magnetic studies of AST microspheres

To explore the chemical states of Sn bulk-doped TiO₂ in detail, ¹¹⁹Sn Mössbauer spectra were recorded. The nuclear ground and excited

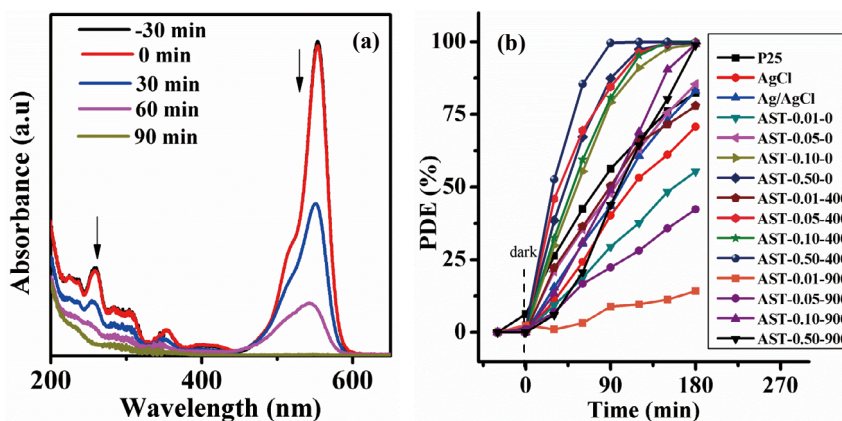


Figure 6. UV-vis spectra of filtrate solution of RhB isolated from photocatalysis with AST-0.50-400 sample (a), PDE vs irradiation time (b) of pristine P25, AgCl, Ag/AgCl and AST samples under visible light irradiation in an aqueous medium.

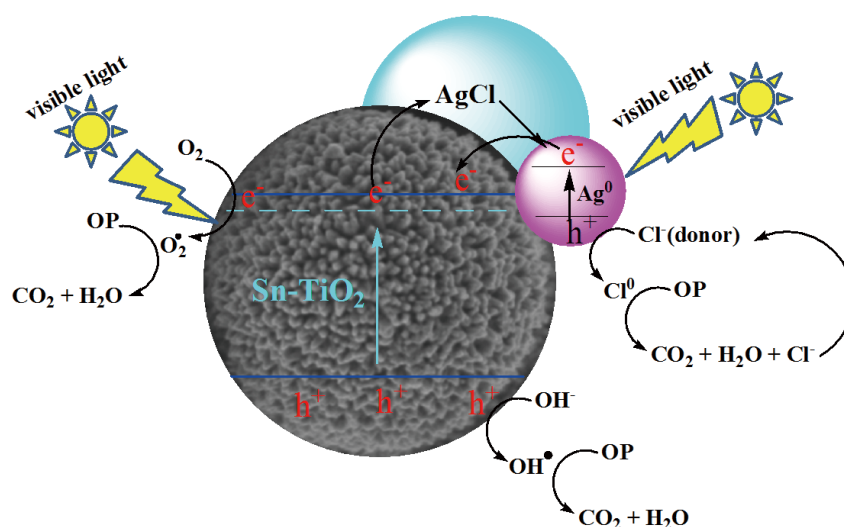


Figure 7. Proposed visible light photocatalytic reaction mechanism of AST catalyst.

levels involved in the Mössbauer transition were shifted or split because of the electrostatic interactions between the nuclear charge and the surrounding electric charge [27]. As shown in Figure 8a-c, clear signals were seen in AST at various levels of AgCl content and calcination temperatures. Mössbauer spectra of all as prepared samples were decomposed into two doublets with different quadrupole splitting and isomer shift values of around $0.08 - 0.13 \text{ mm s}^{-1}$ (D1) and $0.08 - 0.11 \text{ mm s}^{-1}$ (D2), indicating the surface layer-located and bulk-doped Sn^{4+} ions of the hierarchical TiO_2 grains, respectively. They are in paramagnetic states with different quadrupole interactions as an octahedral structure. D1 has a little higher IS and QS values [11]. However, we do not clarify whether the induced magnetism

is existing or not for as prepared and $400 \text{ }^\circ\text{C}$ annealed samples. It is considered that AgCl lock is interacting on the Sn- TiO_2 surface; even though various level of AgCl content hasn't affect the chemical states in Sn- TiO_2 lattice sites.

Moreover, when the surface chemical states of Sn in TiO_2 were examined by conversion electron ^{119}Sn Mössbauer spectroscopy (CEMS) [28], the typical CEMS spectrum was observed for AST-0.01-0 sample (Figure 9). We observed two doublets with IS and QS values are presented in Table 1, while doublet1/doublet2 (D1/D2) ratio of CEMS is higher than the transmission Mössbauer spectra. D1 indicates Sn species doped with TiO_2 surface lattice with some defects sites and D2 reflects Sn species perfectly doped in bulk lattice. All

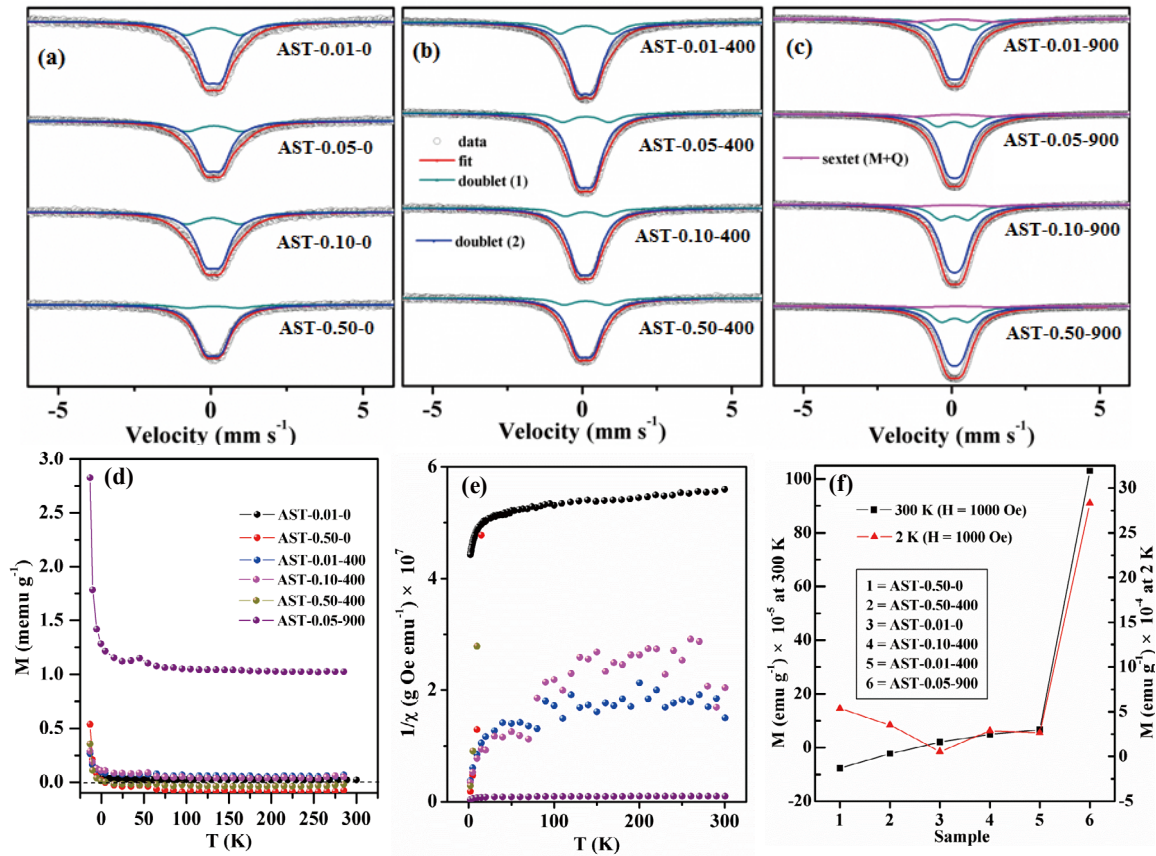


Figure 8 Room-temperature ^{119}Sn Mössbauer spectra of AST samples (a)-(c), temperature dependence of magnetization plots measured for the temperature range of 2 to 300 K (d), variation in inverse magnetization with temperature (e), comparison study between magnetization values with selected samples at 2 and 300 K (f).

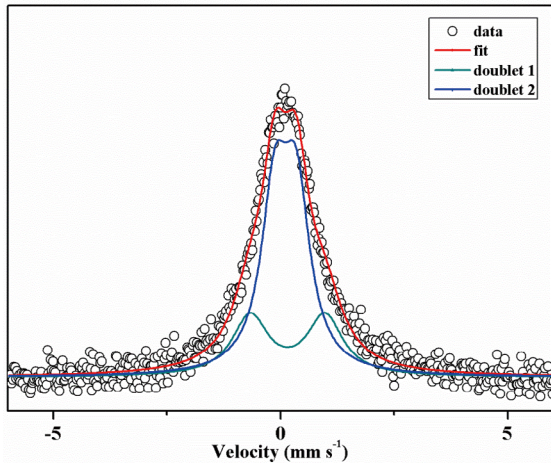


Figure 9. Conversion electron ^{119}Sn Mössbauer spectrum (CEMS) of typical AST-0.01-0 sample.

Mössbauer spectra have been decomposed using the restricted FWHM of D1 and D2. This deconvolution is found to be reasonable

because the D1 intensity decreased with the increase of AgCl contents. The annealed samples showed the narrow FWHM of peaks as compared with as prepared ones. However, the high temperature (900°C) calcined samples (AST-x-900) showed the broadening in the foot of Mössbauer peaks although the Sn states in bulk were assumed to have the peaks with the same FWHM of peaks for 400°C calcined samples. We decomposed them by adding one magnetic sextet component with two quadrupole doublets (Figure 8c). More complex structure of the powder grains was observed, which may be due to the formation of different configurations of $\text{Ti}(\text{Sn})\text{O}_2$ particles with structural defect sites or with 2 Sn atoms substituted at 2 Ti atom sites. These results indicate that the two components are assumed as Ti present in bulk and surface layers of the grains. At high calcinations of 900 °C, samples where we observed the weak magnetism, the $\text{Ti}(\text{Sn})\text{O}_2$ oxides may appear on the parts of surface of the grains produced by the reaction,

oxidization, or decomposition of AgCl.

However, the magnetic studies of AST microspheres have been hitherto unexplored. Figure 8d shows the magnetic properties as function of magnetic field versus various temperatures (M-T) observed for some of the selected samples. The high level AgCl contained samples of AST-0.50-0 and AST-0.50-400 showed diamagnetic properties at room temperature. The magnetization increased monotonically with the temperature decrease nearly 13 K, indicating the transfer from the diamagnetic or very weak ferromagnetic nature into weak ferromagnetic background. Here we didn't observe smooth reciprocal susceptibility curve (Figure 8e) for all selected samples, which may be attributed to various magnetic sites present in these samples. From Figure 8f, among all selected samples AST-0.05-

900 sample showed high magnetic response at 300 and 2 K; it may be due to generation of amorphous nature, oxygen vacancies and structural defects induced magnetism [29, 30]. However, these sites don't influence the photocatalytic activity, because the particle sizes increased and oxidized form of SnO₂ impurity inhibits the photocatalytic activity of AST-x-900 samples. Because of above reasons we are unable to get the good correlation study between magnetic and photocatalytic properties for AST samples. Moreover, AgCl NPs involved the predominant role of photocatalytic behavior as supported with Sn-TiO₂ microspheres.

5. Iron oxide coupled and doped titania nanocomposites

5.1. Preparation of iron oxide coupled

Table 1. CEMS and commercial ¹¹⁹Sn Mössbauer spectral data of AST-0.01-0 sample.

Parameters	CEMS	commercial
χ^2	618.47	803.97
normalized χ^2	1.23	1.60
D1	32.0 %	27.5 %
IS (mm s ⁻¹)	0.15	0.08 (0.009)
QS (mm s ⁻¹)	1.64	1.77 (0.029)
LW	0.96	1.07
D2	68.0 %	72.5 %
IS (mm s ⁻¹)	0.11	0.09 (0.002)
QS (mm s ⁻¹)	0.47	0.52 (0.006)
LW	0.72	0.81
D1/D2	0.47	0.38

and doped titania nanocomposites

Firstly, about 5 mol reddish brown titanium nitrate aqueous solution was prepared [6]. In order to prepare various Fe loaded titania, 0.5, 1.0, 2.0, 3.0 and 4.0 M ferric nitrate (100 mL) aqueous solutions were introduced separately into the titanium nitrate aqueous solutions under magnetic stirring. Then 100 mL of oxalic acid solution (0.6 M) was added drop wise within 2 h under magnetic stirring to ensure complete precipitation. The resultant suspension was transferred into teflon lined stainless steel autoclave, sealed and heated upto 110 °C for 4 h with a pressure maintained

at 18 psi. Finally, the precipitates were filtered, washed with distilled water followed by ethanol, and dried in air at 90 °C for 12 h. The dried precipitates were calcined at 400 °C for 4 h in a muffle furnace to get iron oxide coupled and doped titania nanocomposites. These nanocomposites are denoted as S1, S2, S3, S4 and S5, prepared using 0.5, 1.0, 2.0, 3.0 and 4.0 M ferric nitrate (100 mL) in titanium nitrate solutions, respectively. Experimental results reported for pure anatase TiO₂ sample in our previous paper [7], are referred for comparison.

5.2. ^{57}Fe Mössbauer and EPR spectroscopies characterization

^{57}Fe Mössbauer spectroscopic measurements were used in determining the chemical state of iron in the prepared nanocomposites. As shown in Figure 10a, the spectral peaks of S1-S5 samples could be fitted by the simple addition of spectra for iron oxide coupled and doped TiO_2 in equal proportion. It is noteworthy that the QS for the surface-coupled and bulk-doped iron oxide are different. The doublets were assigned to Fe^{3+} states and showed $\text{IS} = 0.35\text{-}0.38 \text{ mm s}^{-1}$ and $\text{QS} = 0.50\text{-}0.61 \text{ mm s}^{-1}$ for iron oxide doped TiO_2 , whereas $\text{IS} = 0.33\text{-}0.36 \text{ mm s}^{-1}$ and $\text{QS} = 0.94\text{-}1.08 \text{ mm s}^{-1}$ for iron oxide surface coupled TiO_2 , indicates surface iron oxide having a larger structural degree of freedom as compared to that of doped iron oxide. It may be due to the formation of higher symmetric state, and oxygen vacancies or structural defects [27]. The peak area of bulk doped and coupled iron sites are 18.4-45.7 % and 54.3-81.6 % for S1, S3, S4 and S5 samples, respectively. It could be concluded that bulk doped iron sites are smaller than surface coupled iron sites, however contrast behavior was observed for S2 sample. Our group recently reported paramagnetic doublet for Fe doped and Fe-Sn codoped TiO_2 by a soft-chemical solution process [31, 32]. Alternatively, the value of isomer shift for the superparamagnetic doublet is around 0.34 mm s^{-1} with larger QS values of the sample with particle diameter of less than 10 nm, which is larger than those of the amorphous samples [33]. This could be concluded that the nanoparticles begin to show superparamagnetic behavior in the case of hematite. The superparamagnetic behavior [34]

of these nanoparticles leads to a complete lack of magnetic hyperfine splitting of the spectrum and represents in quadrupole doublet with IS of $\sim 0.34 \text{ mm s}^{-1}$ and a QS of $\sim 0.99 \text{ mm s}^{-1}$ [35]. These results indicate that bulk doped Fe^{3+} ions are substitutionally introduced into TiO_2 crystal at Ti^{4+} sites and superparamagnetic Fe_2O_3 nanocrystals are in coupled state with titania surface matrix.

Figure 10b exhibits the EPR spectra of S1-S5 samples recorded at room temperature. There appears broad signals with respect to gyromagnetic factor (g) at 2.00-2.04 and 4.33-4.47 (Table 2), whereas no such signals were observed for amorphous Fe_2O_3 , $\alpha\text{-Fe}_2\text{O}_3$, TiO_2 , and a physically mixed oxide (10 wt% $\text{Fe}_2\text{O}_3/\text{TiO}_2$) [36]. The resonance lines at 2.00 ($\Delta\text{Hpp} \sim 60 - 98 \text{ G}$), 2.00-2.16 ($\Delta\text{Hpp} \sim 1000\text{-}800 \text{ G}$) and 4.30 are usually attributed to the isolated octahedral Fe^{3+} in anatase, Fe^{3+} in iron oxides-type clusters and isolated rhombic Fe^{3+} ions segregated on the TiO_2 surfaces, respectively [27, 37]. It suggests that iron oxide such as Fe_2O_3 particles are present on the TiO_2 surfaces and furthermore isolated rhombic Fe^{3+} ions doped in TiO_2 bulk in S1-S5 samples. As Fe content increased, both the intensity and line width increased. This is because the increase in iron oxide loading would increase the magnetic interaction between Fe^{3+} ions.

5.3. Magnetic characterizations

Magnetic aspects of nanocomposites were investigated by room temperature vibrating sample magnetometric (VSM) and temperature dependent magnetization measurements. Room temperature magnetization curves of the as-prepared S1-S5 nanocomposites are presented in Figure 11a. The curve of the samples

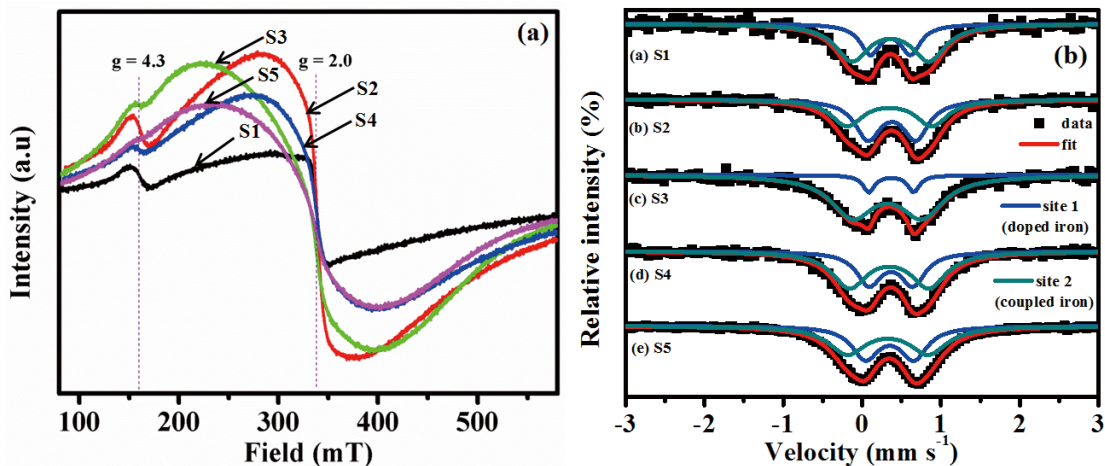


Figure 10. ^{57}Fe Mössbauer (a) and EPR (b) spectra of S1-S5 samples at room temperature.

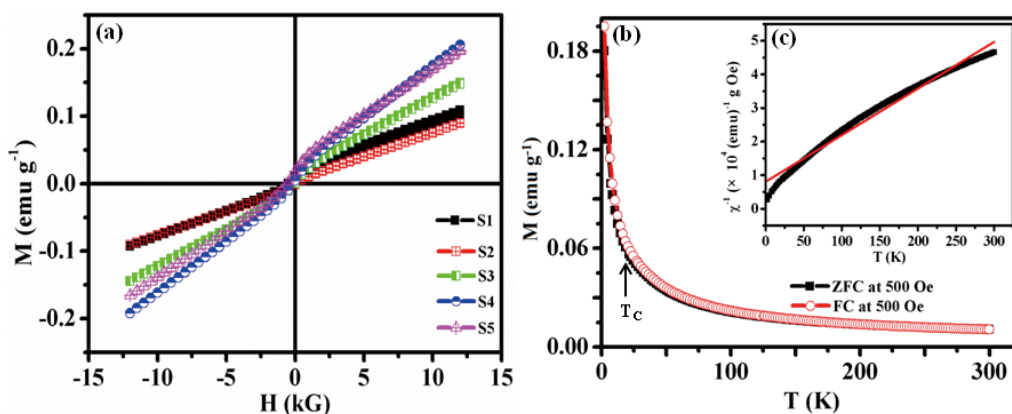


Figure 11. Magnetization curve of S1-S5 samples at room temperature (a), temperature dependence of ZFC/FC magnetization plots measured between 2 and 300 K (b), where the critical phase transition temperature (T_c) is indicated on the ZFC/FC data set, and variation in inverse magnetization with temperature (c) for the S5 sample.

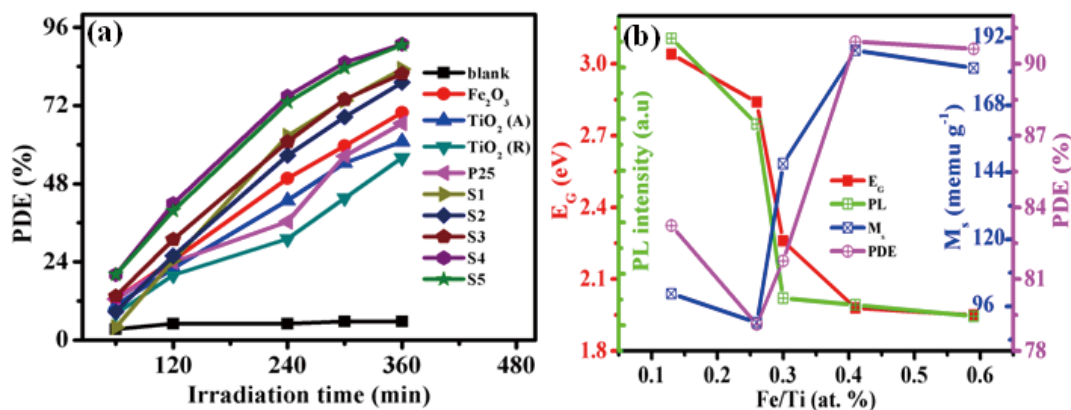


Figure 12 PDE of MB blank solution, with reference catalysts and prepared S1-S5 samples under visible light ($\lambda > 480$ nm) irradiation at various time intervals in water (a) and variation of band gap energy (E_G), PL intensity of emission band, magnetization (M_s) and PDE values of S1-S5 samples with different Fe/Ti atomic ratio level obtained from ICP results (b).

makes very weak saturation magnetization (M_s) even at a magnetic field of 15 kG, and no hysteresis is found. It can be understood that the as-prepared nanocomposites perform weak paramagnetic with superparamagnetic behavior as noticed from both magnetic and Mössbauer studies. Literature reports indicated that the superparamagnetic TiO_2 - Fe_2O_3 composites showed rapid aggregation under the influence of a magnetic field, which can be useful for separation of these particles after remediation and in applications [38]. In case the system is focused for magnetic recovery and regeneration, then the M_s value of the iron oxides is anticipated to be no less than 1 emu g^{-1} , so as to separate using external magnetic field [39]. In the present case, the M_s value ($90.2 - 187.6 \times 10^{-3} \text{ emu}$

g^{-1}) of nanocomposites are very weak with absence of coercivity (H_c) and remanence (M_r), which makes it very difficult to re-collect the composite particles through an external magnetic field. This weak superparamagnetic behavior is also an indication that iron oxide is not separately present in nanocomposites, but is in coupled state with TiO_2 surface matrix. Temperature-dependent zero field cooling (ZFC) and field cooling (FC) magnetization data for typical S5 sample is shown in Figure 11b at 500 Oe. In proper scanning between 2 to 300 K, magnetization decreased appreciably upto T_c nearer to 23 K then it has slowly decreased. No significant difference was observed between ZFC and FC data, showing clear evidence of paramagnetism, while magnetization values are less than 0.06

emu g⁻¹ at from the 23 to 300 K temperature range. It could be concluded EPR and ⁵⁷Fe Mössbauer spectroscopic measurements at room temperature supported the existence of weak superparamagnetism. Further evidence of the weak superparamagnetism and the possible very weak ferromagnetic behavior at below T_c = 23 K can be observed by inspection of magnetic moment vs. temperature plot and the reciprocal susceptibility χ^{-1} for sample S5 (Figure 11b, c).

5.4. Photocatalytic activity characterization

To evaluate the photocatalytic activity of S1-S5 nanocomposites, methylene blue (MB) solution was used as the model. The temporal UV-Vis spectral changes of MB aqueous solution during the photocatalytic degradation reactions are depicted in Figure 12. As seen from the figure, when the MB solution was irradiated under the visible light, the main MB absorbance markedly decreased with irradiation time and almost ~91% disappeared in about 360 min of irradiation. MB solution could not be degraded in the presence of prepared catalyst under the dark conditions (Figure 12a), signifying that MB degradation in the present study is indeed through a photocatalytic process. Comparison experiments demonstrated that MB photolysis (without any catalyst) was very slow. Further compared to pure Fe₂O₃, rutile TiO₂, anatase TiO₂ and P25 nanoparticles, the photocatalytic activity (Figure 12a) of our samples are efficient, which may be due to the compositional modification. Correlation analysis was performed between iron content, photocatalytic activity, optical and magnetic behavior of prepared samples. The band gap energy and PL peak intensity values are correlated with Ms and photocatalytic activity results for the as-prepared samples is illustrated in Figure 12b. Therefore, it can be concluded that implantation of iron oxides subsequent electronic energy levels in the S1-S5 samples are mainly responsible for optical, magnetic and photocatalytic activity of present samples. It has been shown that high levels of iron loaded TiO₂ can strongly reduce the band gap energy and PL intensity, resulting in the formation of new trap level below the conduction band of TiO₂ [40]. This will reduce e⁻-h⁺ recombination rate and alternatively lead to high level of electron transformation between neighboring metal oxides due to synergetic effect [41], making the catalyst

more efficient in photocatalytic activity and strong magnetic behavior in metal oxides coupled semiconductor nanocomposites [6, 7, 42].

6. Photoinduced formation of iron(III) oxide:titania nanoparticles

6.1. Photolysis procedure of precursor complex with titania in aqueous medium

The interfacial electron transfer (IFET) process was evaluated by photoreduction of [Fe^{III}(bipy)₂Cl₂][Fe^{III}Cl₄] precursor complex (251 μM) with TiO₂ NPs (200 mg) using PE.ILC CERMAX xenon illumination system model LX 175/ 300 attached with CX-04E power supply (10 A) and with different cut off filters ($\lambda \geq 380, 400, 440, 480$ and 520 nm) were used as the light source. The distance between the lamp and the solution was 8.0 cm. Photolysis experiments were performed in a dark box. In a typical photocatalytic experiment, 200 mg of TiO₂ NPs was dispersed in an 80 mL precursor complex (251 μM) aqueous medium in a 100 mL glass beaker at room temperature. Then the suspension was kept in darkness and magnetically stirred for 30 min to reach the adsorption–desorption equilibrium on solid catalyst. Prior to irradiation, the solution was continuously stirred with a magnetic stirrer for a thorough mixing. About 3 mL of aliquots were periodically taken out from the suspension at 0, 5, 15, 30, 60 and 120 min time intervals and centrifuged (15,000 rpm, 5 min) to separate the solution and characterized the product. The supernatants were measured by GBC Cintra UV-vis spectrophotometer. It record UV-vis absorption spectra in the ranges 320-800 nm and 200-400 nm, the second range spectra were observed from the ten times diluted supernatant solutions. In the first range spectra show new peak at 522 nm during various irradiation times. The absorbance values were noted at 522 nm for the estimation of photochemical product. In order to diminish the experimental error, the experiments were repeated at least three times for the same sample and noted the mean value.

6.2. Photoinduced interfacial electron transfer process under visible light

The surface-adduct $\equiv\text{TiO}_2//\text{Fe}_{\text{sc}}^{\text{III}}$ could enhance the IFET process in irradiation system. Generally, titania has a large band gap energy ($E_G = 3.2$ eV) and it can be trigger by UV light irradiation. However, the surface adducts observed visible light and promotes the IFET

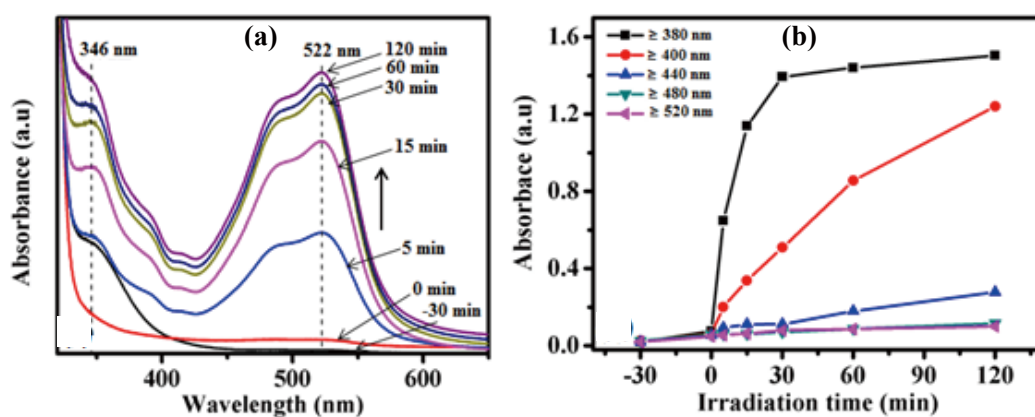


Figure 13. Electronic absorption spectra of precursor complex $[\text{Fe}^{\text{III}}(\text{bipy})_2\text{Cl}_2][\text{Fe}^{\text{III}}\text{Cl}_4]$ with ST01 aqueous solution after near-UV light ($\lambda \geq 380 \text{ nm}$) irradiation at different time (a). Absorbance change at 522 nm vs irradiation time for the precursor complex with ST01 aqueous solution by using different cut off filters (b).

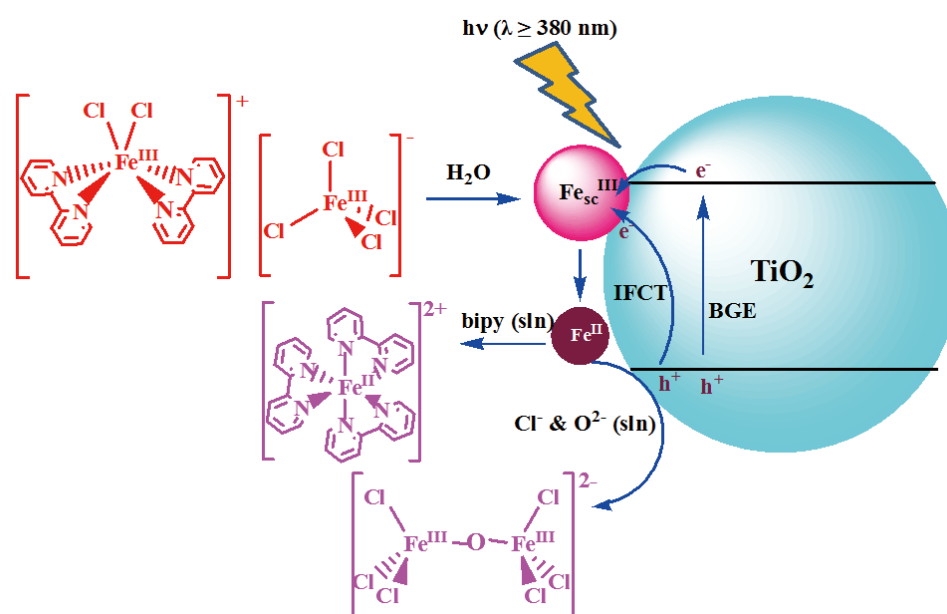


Figure 14. Photolysis mechanism of precursor complex with TiO_2 NPs under near-UV light irradiation in water, involving interfacial electron transfer (IFET) and multi-electron reduction processes (where BDE is the band gap excitation).

reaction under visible light irradiation. The electronic absorption spectra of precursor complex with TiO_2 NPs under near-UV light are in Figure 13a. These observations indicate that the precursor complex mostly decomposes within 30 min under near-UV light irradiation. Besides it was confirmed from Figure 13b that there was a regular increment in attain absorption change at 522 nm. This result concludes that among all reaction conditions the precursor complex// TiO_2 NPs under near-UV light irradiation system shows an enhanced

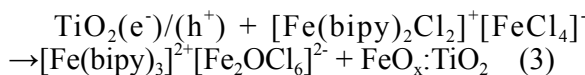
IFET process and hence well reduction occurred. The various types of TiO_2 NPs play important role in the surface interaction and photocatalytic performance. We compare four different types of TiO_2 NPs for instance anatase, rutile, ST01 and P25 in both dark and visible light conditions. The rutile phase was performed well than that of other kind of titania NPs, while no reaction was observed in blank solution. It indicates that the rutile TiO_2 NPs could strongly interact with precursor complex to promote the formation of solution

products *via* IFET process.

We have proposed the IFET mechanism of photoinduced reduction of iron(III) precursor complex with TiO₂ under near-UV light irradiation resulting in the formation of more stable Fe(II)-bipy complex. The photoreduction of Fe^{III} to Fe^{II} is the most significant mode of photoreduction of precursor complex. Photoreactive LMCT state is populated to produce Fe^{II}_{sol} species in Eq. 3. From Figure 14, the photolysis reaction in presence of TiO₂ NPs alters the effect leading to insertion of Fe(III) ions on surface of TiO₂ NPs to form surface adduct. This surface adducts acts as a co-catalyst on this process [43]. The surface adduct could create new electronic energy level on TiO₂ surface interface. Thus the surface impurity level was enhanced and the electron transfer from valance band (VB) of near-UV or visible light excited TiO₂ to the lowest unoccupied molecular orbital (LUMO) of surface complex (Fe^{III}_{sc}) and simultaneously reduction of Fe^{III}_{sc} to Fe^{II} ions. Finally Fe^{II} ions have coordinated with the bipy ligand to form stable [Fe^{II}(bipy)₃]²⁺ complex cation. However, trapped holes in coordination with some of Fe^{II} species to produce [Fe₂OCl₆]²⁻ complex anion. Since free bipy ligand and Cl- and O²⁻ ions could form during decomposition of precursor complex under near-UV or visible light irradiation. The LMCT and photoinduced IFET transitions were observed for precursor complex with presence of TiO₂ NPs under near-UV or visible light irradiation in aqueous medium as given in Eqs. (1)- (3). The overall schematic diagram is in Figure 15.

Path 1: LMCT mechanism (less efficient)
 $[\text{Fe}(\text{bipy})_2\text{Cl}_2]^+[\text{FeCl}_4]^- + h\nu \rightarrow \text{LMCT} \rightarrow \text{Fe}^{\text{II}}_{\text{sol}} \text{ complex} \quad (1)$

Path 2: IFET mechanism (high efficient)
 $\text{TiO}_2 + h\nu \rightarrow \text{TiO}_2(e^-)/(h^+) \quad (2)$



6.3. Identification of the visible light induced products

The chemical states and structure of precursor complex, reference complex and reduction products could identify by ⁵⁷Fe Mössbauer spectroscopy. The photoirradiated samples were isolated from photolysis of precursor complex with ST01 NPs under near-UV and visible light irradiations by slow evaporation method. The Mössbauer spectrum of precursor complex consists of two quadrupole doublets (Table 2), which are attributed to [Fe^{III}(bipy)₂Cl₂]⁺ and [Fe^{III}Cl₄]⁻ complex ion sites, respectively. While two doublets observed for reference complex (Figure 3b), which are corresponding to Fe(II) state of [Fe^{II}(bipy)₃]²⁺ and Fe(III) sites of [Fe^{III}₂OCl₆]²⁻ complex ion sites. The IS and QS values (Table 1) of precursor and reference complexes were good agreement with previous observations [44-46]. Moreover, three components were observed for the photoproduct (λ ≥ 440 nm irradiation system) as presented in Table 2. The Mössbauer parameters of last two components are almost similar with reference complex (sites 3 and 4). While, the first component similar with [FeCl₄]⁻ (site 2) ion. However, the IS value of photoproduct is smaller than IS value of precursor complex. This could indicate that un-reacted precursor complex surround with some solvent molecules in photochemical product (λ ≥ 440 nm irradiation system). This result concludes that visible light (λ ≥ 440 nm) irradiation system could create less excited electron on precursor complex//TiO₂ NPs interface.

Moreover, Mössbauer spectrum of

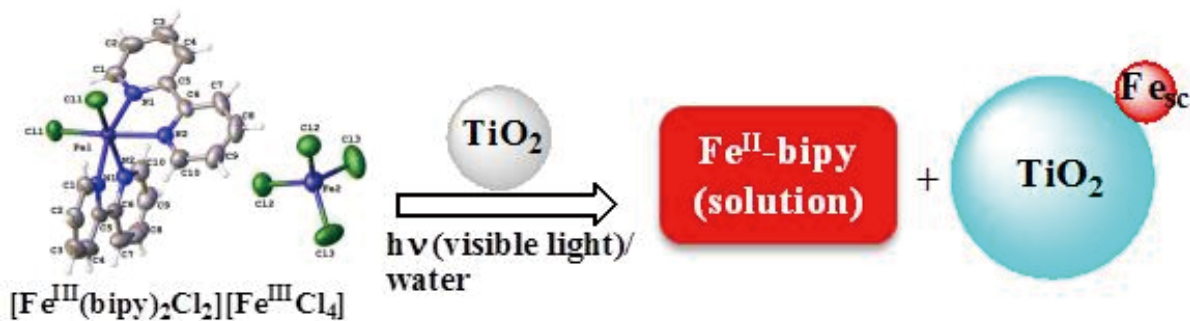


Figure 15. The overall schematic diagram of photolysis of precursor iron(III) complex with TiO₂ nanoparticles in aqueous medium.

Table 2. Room temperature ^{57}Fe Mössbauer spectroscopy parameters of precursor complex, reference complex and photochemical products obtained from $\lambda \geq 380$ and 440 nm irradiation systems.

sample	site	IS ^[a]	QS ^[b]	A ^[c]
precursor complex	doublet (site 1) ^[d]	0.36	0.52	60.4
	singlet (site 2) ^[e]	0.34	-	40.6
reference complex	doublet 1 (site 3) ^[f]	0.20	1.21	36.4
	doublet 2 (site 4) ^[g]	0.27	0.29	63.6
photoproduct ($\lambda \geq 440$ nm)	singlet (site 2) ^[e]	0.21	-	13.0
	doublet 1 (site 4) ^[g]	0.23	0.29	56.2
	doublet 2 (site 3) ^[f]	0.26	0.75	30.7
	doublet 1 (site 4) ^[g]	0.27	0.29	93.4
photoproduct ($\lambda \geq 380$ nm)	doublet 1 (site 4) ^[g]	0.27	0.29	93.4
	doublet 2 (site 3) ^[f]	0.40	1.01	6.6

[a] IS = isomer shift (mm s^{-1}), [b] QS = quadrupole shift (mm s^{-1}), [c] A = peak area (%), [d] site 1 = $[\text{Fe}^{\text{III}}(\text{bipy})_2\text{Cl}_2]^+$, [e] site 2 = $[\text{Fe}^{\text{III}}\text{Cl}_4]^-$, [f] site 3 = $[\text{Fe}^{\text{III}}_2\text{OCl}_6]^{2-}$, [g] site 4 = $[\text{Fe}^{\text{II}}(\text{bipy})_3]^{2+}$...

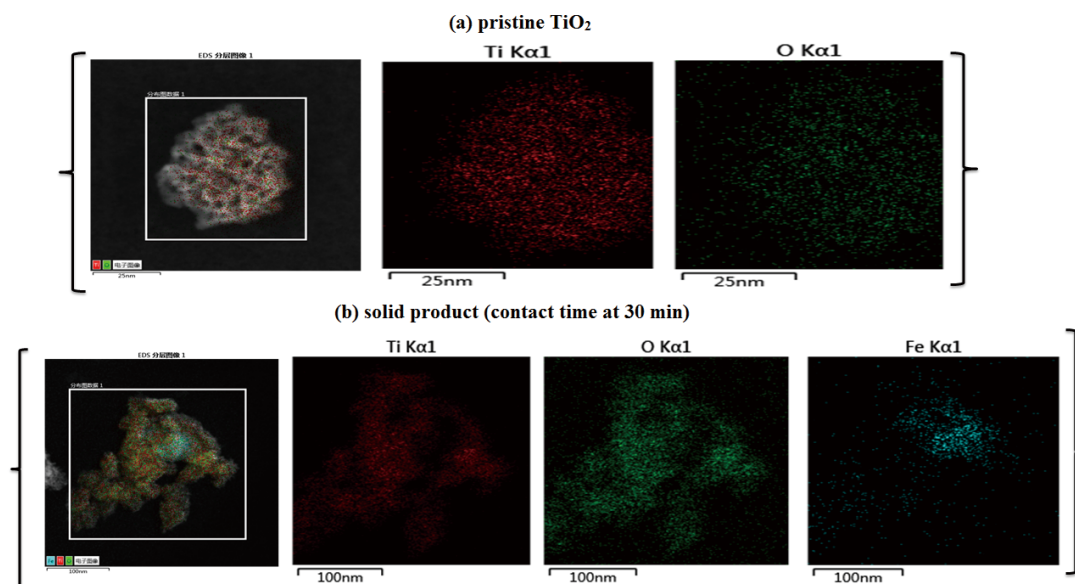


Figure 16. Elements mapping of pristine TiO₂ (a) and solid product at 30 min contact time in dark (b).

photoproduct obtained from near-UV light irradiation system clearly showed two components such as $[\text{Fe}^{\text{III}}_2\text{OCl}_6]^{2-}$ (site 3) and $[\text{Fe}^{\text{II}}(\text{bipy})_3]^{2+}$ (site 4). While site 4 (93.4%) is most predominant component than site 3

(6.6%). This is conclude that the iron(III)-bipy precursor complex was effectively reduced with TiO₂ NPs under near-UV light irradiation via IFET process to form stable iron(II)-bipy photochemical product. On the other hand, we

could find some interesting characterization of surface-adduct $\text{FeO}_x\cdot\text{TiO}_2$ (solid product), the detailed discussion about solid product should be reported in our future paper. However, Figure 20 shows typical element mappings of pristine TiO_2 and solid product which was isolated from precursor complex with TiO_2 in aqueous medium at 30 min contact time in dark. It's one of the evidence for solid product and Fe atoms dispersed among the TiO_2 crystalline phase in solid product.

The states of surface-implanted and bulk-doped iron with TiO_2 in more detail on account of ^{57}Fe Mössbauer spectra [37]. The IS and QS values of all-as prepared samples are not consistent with Mössbauer parameters of precursor complex, it indicates that precursor complex does not simply excites in all as-prepared samples. In conclusion, interfacial electron transfer process between $[\text{Fe}^{\text{III}}(\text{bipy})_2\text{Cl}_2][\text{Fe}^{\text{III}}\text{Cl}_4]$ complex and TiO_2 NPs to form stable reduction product of iron(II)-bipy complex by ^{57}Fe Mössbauer spectroscopy. However, the IFET reaction was mainly controlled by following factors: (i) irradiation time, (ii) various region of light, and (iii) various crystalline types of TiO_2 NPs. These results are important for improving and understanding the IFET property of semiconductor photocatalysts with metal complex and also new route to prepare iron oxide deposited titania by photochemical method, which may be useful for the construction of efficient photochemical energy conversion and photocatalytic systems.

7. Conclusion

This review covers Mössbauer spectroscopic, magnetic and photocatalytic investigations of tin or iron-based titania nanocomposites performed by our group. Using simple hydrothermal, we prepared tin-based titania, otherwise iron oxide coupled titania was prepared by photochemical method. Mössbauer spectroscopy has matured into one of the classical techniques for tin or iron-based titania structural and magnetic characterization. Mössbauer spectroscopic results provided strong evidence the relationship between the structural, magnetic and catalytic properties of tin or iron-based titania. With the efficient visible light absorption and high photocatalytic activity and stability, the tin or iron-based TiO_2 nanocomposites have promising application in photocatalysis for degradation of organic pollutants and purification of water. We

strongly believe that our work would contribute toward the fundamental understanding of structural and magnetic properties of tin or iron-based TiO_2 nanocomposites and would be useful for inexpensive nontoxic photocatalyst materials.

Acknowledgment

J. Wang is grateful to National Natural Science Foundation of China (NSFC) (No. 21476232). This work was also partially supported by the China Ministry of Science and Technology (No. 2016YFA0202804). A. S. Ganeshraja acknowledges the CAS President's International Fellowship Initiative (PIFI) programme for a postdoctoral researcher funded by the Chinese Academy of Sciences (No. 2016PT023) and International Young Scientists Research Fund project funded by the NSFC (No. 2161101071).

References

- [1] M. Dahl, Y. Liu, Y. Yin: Composite titanium dioxide nanomaterials, *Chem. Rev.*, **2014**, *114*, 9853–9889.
- [2] L. Sun, W. Wu, S. Yang, J. Zhou, M. Hong, X. Xiao, F. Ren and C. Jiang: Template and silica interlayer tailorable synthesis of spindle-like multilayer $\alpha\text{-Fe}_2\text{O}_3/\text{Ag}/\text{SnO}_2$ ternary hybrid architectures and their enhanced photocatalytic activity, *ACS Appl. Mater. Interfaces*, **2014**, *6*, 1113–1124.
- [3] H. Honda, A. Ishizaki, R. Soma, K. Hashimoto, A. Fujishima: Application of photocatalytic reaction caused by TiO_2 film improved the maintenance factor of lighting system, *J. Illum. Eng. Soc.*, **1998**, *27*, 42–49.
- [4] J. S. Im, S. K. Lee, Y. S. Lee: Cocktail effect of Fe_2O_3 and TiO_2 semiconductors for a high performance dye-sensitized solar cell, *Appl. Surf. Sci.*, **2011**, *257*, 2164–2169.
- [5] X. Li, K. Zhu, J. Pang, M. Tian, J. Liu, A. I. Rykov, M. Zheng, X. Wang, X. Zhu, Y. Huang, B. Liu, J. Wang, W. Yang, T. Zhang: Unique role of Mössbauer spectroscopy in assessing structural features of heterogeneous catalysts, *Applied Catalysis B: Environmental*, **2018**, *224*, 518–532.
- [6] A. S. Ganeshraja, A. S. Clara, K. Rajkumar, Y. Wang, Y. Wang, J. Wang, K. Anbalagan: Simple hydrothermal synthesis of metal oxides coupled nanocomposites: Structural, optical, magnetic and photocatalytic studies, *Appl. Surf. Sci.*, **2015**, *353*, 553–563.
- [7] A. S. Ganeshraja, S. Thirumurugan, K. Rajkumar, K. Zhu, Y. Wang, K. Anbalagan, J. Wang: Effects of structural, optical and ferromagnetic states on the photocatalytic activities of Sn-TiO_2 nanocrystals, *RSC Adv.*, **2016**, *6*, 409–421.

- [8] A. S. Ganeshraja, K. Rajkumar, K. Zhu, X. Li, S. Thirumurugan, W. Xu, J. Zhang, M. Yang, K. Anbalagan, J. Wang: Facile synthesis of iron oxide coupled and doped titania nanocomposites: Tuning of physicochemical and photocatalytic properties, *RSC Adv.*, **2016**, *6*, 72791–72802.
- [9] A. S. Ganeshraja, S. Thirumurugan, K. Rajkumar, J. Wang, K. Anbalagan: Ferromagnetic nickel(II) imidazole-anatase framework: An enhanced photocatalytic performance, *J. Alloys Compd.*, **2017**, *706*, 485–494.
- [10] A. S. Ganeshraja, M. Yang, K. Nomura, S. Maniarasu, G. Veerappan, T. Liu, J. Wang: ¹¹⁹Sn Mössbauer and ferromagnetic studies on hierarchical tin- and nitrogen-codoped TiO₂ microspheres with efficient photocatalytic performance, *J. Phys. Chem. C*, **2017**, *121*, 6662–6673.
- [11] A. S. Ganeshraja, K. Zhu, K. Nomura, J. Wang: Hierarchical assembly of AgCl@Sn-TiO₂ microspheres with enhanced visible light photocatalytic performance, *Appl. Surf. Sci.*, **2018**, *441*, 678–687.
- [12] A.S. Ganeshraja, M. Yang, W. Xu, K. Anbalagan, J. Wang: Photoinduced interfacial electron transfer in 2,2'-bipyridyl iron(III) complex-TiO₂ nanoparticles in aqueous medium, *ChemistrySelect*, **2017**, *2*, 10648–10653.
- [13] C. Wang, C. Shao, X. Zhang, Y. Liu: SnO₂ nanostructures-TiO₂ nanofibers heterostructures: Controlled fabrication and high photocatalytic properties, *Inorg. Chem.*, **2009**, *48*, 7261–7268.
- [14] P. B. Fabritchnyi, M. V. Korolenko, M. I. Afanasov, M. Danot, E. Janod: Mössbauer characterization of tin dopant ions in the antiferromagnetic ilmenite MnTiO₃, *Solid State Commun.*, **2003**, *125*, 341–346.
- [15] P. Chetri, P. Basyach, A. Choudhury: Exploring the structural and magnetic properties of TiO₂/SnO₂ core/shell nanocomposite: An experimental and density functional study, *J. Solid State Chem.*, **2014**, *220*, 124–131.
- [16] J. Hays, A. Punnoose, R. Baldner, M. H. Engelhard, J. Peloquin, K. M. Reddy: Relationship between the structural and magnetic properties of Co-doped SnO₂ nanoparticles, *Phys. Rev. B*, **2005**, *72*, 075203-1–7.
- [17] S. Zhuang, X. Xu, Y. Pang, H. Li, B. Yu, J. Hu: Variation of structural, optical and magnetic properties with Co-doping in Sn_{1-x}Co_xO₂ nanoparticles, *J. Magnet. Magnet. Mater.*, **2013**, *327*, 24–27.
- [18] P. Wu, B. Z. Zhou, W. Zhou: Room-temperature ferromagnetism in epitaxial Mg-doped SnO₂ thin films, *Appl. Phys. Lett.*, **2012**, *100*, 182405-1–4.
- [19] M. Venkatesan, C. B. Fitzgerald, J. M. D. Coey: Thin films: Unexpected magnetism in a dielectric oxide, *Nature*, **2004**, *430*, 630.
- [20] K. Nomura: Magnetic properties and oxygen defects of dilute metal doped tin oxide based, *Croat. Chem. Acta*, **2015**, *88*, 579-590.
- [21] A. S. Ganeshraja, K. Nomura, J. Wang: ¹¹⁹Sn Mössbauer studies on ferromagnetic and photocatalytic Sn-TiO₂ nanocrystals, *Hyperfine Interact.*, **2016**, *237*, 139.
- [22] L. Aldon, P. Kubiak, A. Picard, J. -C. Jumas: Size particle effects on lithium insertion into Sn-doped TiO₂ anatase, *Chem. Mater.*, **2006**, *18*, 1401–1406.
- [23] G. Luo, X. Jiang, M. Li, Q. Shen, L. Zhang, H. Yu: Facile fabrication and enhanced photocatalytic performance of Ag/AgCl/rGO heterostructure photocatalyst, *ACS Appl. Mater. Interfaces*, **2013**, *5*, 2161–2168.
- [24] L. Sun, R. Zhang, Y. Wang, W. Chen: Plasmonic Ag@AgCl nanotubes fabricated from copper nanowires as high-performance visible light photocatalyst, *ACS Appl. Mater. Interfaces*, **2014**, *6*, 14819–14826.
- [25] R. Dong, B. Tian, C. Zeng, T. Li, T. Wang, J. Zhang: Ecofriendly synthesis and photocatalytic activity of uniform cubic Ag@AgCl plasmonic photocatalyst, *J. Phys. Chem. C*, **2013**, *117*, 213–220.
- [26] H. Xu, H. M. Li, J. Xia, S. Yin, Z. Luo, L. Liu, L. Xu: One-pot synthesis of visible-light-driven plasmonic photocatalyst Ag/AgCl in ionic liquid, *ACS Appl. Mater. Interface*, **2011**, *3*, 22–29.
- [27] M. Liu, X. Qiu, M. Miyauchi, K. Hashimoto: Energy-level matching of Fe(III) ions grafted at surface and doped in bulk for efficient visible-light photocatalysts, *J. Am. Chem. Soc.*, **2013**, *135*, 10064–10072.
- [28] S. S. Sharma, K. Nomura, Y. Ujihira: Characterization of tin oxide films prepared as gas sensors by conversion electron Mössbauer spectrometry, *J. Mater. Sci.*, **1991**, *26*, 4104–4109.
- [29] Y. Liu, Y. Luo, A.A. Elzatahry, W. Luo, R. Che, J. Fan, K. Lan, A.M. Al-Enizi, Z. Sun, B. Li, Z. Liu, D. Shen, Y. Ling, C. Wang, J. Wang, W. Gao, C. Yao, K. Yuan, H. Peng, Y. Tang, Y. Deng, G. Zheng, G. Zhou, D. Zhao: Mesoporous TiO₂ mesocrystals: Remarkable defects-induced crystallite-interface reactivity and their in situ conversion to single crystals, *ACS Cent. Sci.*, **2015**, *1*, 400–408.
- [30] S. D. Yoon, Y. Chen, A. Yang, T. L. Goodrich, X. Zuo, D. A. Arena, K. Ziemer, C. Vittoria, V. G. Harris: Oxygen-defect-induced magnetism to 880 K in semiconducting anatase TiO_{2-δ} films, *J. Phys.: Condens. Matter*, **2006**, *18*, L355–L361.
- [31] Y. Wang, K. Nomura, X. Liu, A. I. Rykov, C. Jin, T. Liu and J. Wang: Structural and magnetic properties of ⁵⁷Fe-doped TiO₂ and ⁵⁷Fe/Sn-codoped TiO₂ prepared by a soft-chemical process, *Eur. J. Inorg. Chem.*, **2016**, 2131–2135.
- [32] J. Wang, Y. Sakai: Mössbauer spectra of iron-doped titanium dioxide fine particles prepared by a soft chemical solution method, *Hyperfine Interact.*, **2013**, *218*, 9–14.
- [33] T. K. Kundu, M. Mukherjee, D.

- Chakravorty, T. P. Sinha: Growth of nano- α - Fe_2O_3 in a titania matrix by the sol-gel route, *J. Mater. Sci.*, **1998**, 33, 1759–1763.
- [34] A. F. Lehlouh, S. H. Mahmood: Mössbauer spectroscopy of Fe_3O_4 ultrafine particles. *J. Magnet. Magnet. Mater.*, **1995**, 151, 163–166.
- [35] M. Grigorova, H. J. Blythe, V. Blaskov, V. Rusanov, V. Petkov, V. Masheva, D. Nihtianova, L. M. Martinez, J. S. Munoz, M. Mikhov: Magnetic properties and Mössbauer spectra of nanosized CoFe_2O_4 powders, *J. Magnet. Magnet. Mater.*, **1998**, 183, 163–172.
- [36] Q. Sun, W. Leng, Z. Li, Y. Xu: Effect of surface Fe_2O_3 clusters on the photocatalytic activity of TiO_2 for phenol degradation in water, *J. Hazard. Mater.*, **2012**, 229–230, 224–232.
- [37] C. Fàbrega, T. Andreu, A. Cabot, J. R. Morante: Location and catalytic role of iron species in TiO_2 :Fe photocatalysts: An EPR study, *J. Photochem. Photobiol. A*, **2010**, 211, 170–175.
- [38] T. Xin, M. Ma, H. Zhang, J. Gu, S. Wang, M. Liu, Q. Zhang: A facile approach for the synthesis of magnetic separable Fe_3O_4 @ TiO_2 core-shell nanocomposites as highly recyclable photocatalysts, *Appl. Surf. Sci.*, **2014**, 288, 51–59.
- [39] W. Wu, C. Jiang, V. A. L. Roy: Recent progress in magnetic iron oxide-semiconductor composite nanomaterials as promising photocatalysts, *Nanoscale*, **2015**, 7, 38–58.
- [40] X. Zhang, Y. Zhu, X. Yang, Y. Zhou, Y. Yao, C. Li: Multifunctional Fe_3O_4 @ TiO_2 @Au magnetic microspheres as recyclable substrates for surface-enhanced Raman scattering, *Nanoscale*, **2014**, 6, 5971–5979.
- [41] J. Xu, Z. Gao, K. Han, Y. Liu, Y. Song: Synthesis of magnetically separable Ag_3PO_4 / TiO_2 / Fe_3O_4 heterostructure with enhanced photocatalytic performance under visible light for photoinactivation of bacteria, *ACS Appl. Mater. Interfaces*, **2014**, 6, 15122–15131.
- [42] Y. Zhang, X. Yu, Y. Jia, Z. Jin, J. Liu, X. Huang: A facile approach for the synthesis of Ag-coated Fe_3O_4 @ TiO_2 core/shell microspheres as highly efficient and recyclable photocatalysts, *Eur. J. Inorg. Chem.*, **2011**, 5096–5104.
- [43] H. Yu, H. Irie, Y. Shimodaira, Y. Hosogi, Y. Kuroda, M. Miyauchi, K. Hashimoto: An efficient visible-light-sensitive Fe(III)-grafted TiO_2 photocatalyst, *J. Phys. Chem. C*, **2010**, 114, 16481–16487.
- [44] E. H. Witten, W. M. Reiff, K. Lazar, B.W. Sullivan, B. M. Foxman: The ferric chloride-alpha.-diamine system. 3. X-ray crystallographic, magnetic susceptibility, and zero- and high-field Mössbauer spectroscopy investigation of bis(2,2'-bipyridine)dichloroiron(2+) tetrachloroferrate(2+): slow paramagnetic relaxation and magnetic ordering of complex bimetallic salts, *Inorg. Chem.*, **1985**, 24, 4585–4591.
- [45] T. Liu, T. Lovell, W. G. Han, L. Noodleman: DFT calculations of isomer shifts and quadrupole splitting parameters in synthetic iron-oxo complexes: applications to methane monooxygenase and ribonucleotide reductase, *Inorg. Chem.*, **2003**, 42, 5244–5251.
- [46] P. Kopel, Z. Travnicek, R. Zboril, J. Marek: Synthesis, X-ray and Mössbauer study of iron(II) complexes with trithiocyanuric acid (ttcH₃): The X-ray structures of $[\text{Fe}(\text{bpy})_3](\text{ttcH}) \cdot 2\text{bpy} \cdot 7\text{H}_2\text{O}$ and $[\text{Fe}(\text{phen})_3](\text{ttcH}_2)(\text{ClO}_4) \cdot 2\text{CH}_3\text{OH} \cdot 2\text{H}_2\text{O}$, *Polyhedron*, **2004**, 23, 2193–2202.